International Journal of Minerals, Metallurgy and Materials
Volume 19, Number 10, Oct 2012, Page 908
DOI: 10.1007/s12613-012-0646-7

Numerical modeling and experimental validation of microstructure in gray cast iron

Masoud Jabbari[1)], *Parviz Davami*[2)], *and Naser Varahram*[2)]

1) Department of Mechanical Engineering, Technical University of Denmark, Kgs. Lyngby 2800, Denmark
2) Department of Materials Science and Engineering, Sharif University of Technology, Tehran 11365, Iran
(Received: 2 August 2011; revised: 26 September 2011; accepted: 11 October 2011)

Abstract: To predict the amount of different phases in gray cast iron by a finite difference model (FDM) on the basis of cooling rate (R), the volume fractions of total γ phase, graphite, and cementite were calculated. The results of phase composition were evaluated to find a proper correlation with cooling rate. More trials were carried out to find a good correlation between the hardness and phase composition. New proposed formulas show that the hardness of gray cast iron decreases as the amount of graphite phase increases, and increases as the amount of cementite increases. These formulas are developed to correlate the phase volume fraction to hardness. The results are compared with experimental data and show reasonable agreement.

Keywords: cast iron; cooling; microstructure; mechanical properties; finite difference method

1. Introduction

Cast iron (CI) remains the most important casting materials with over 70% of the total world tonnage [1]. Based on the shape of graphite, cast iron can be divided into lamellar (flake) and spheroidal (nodular) graphite iron. In recent years, the numerical simulation and computer aided modeling of casting solidification are developed. Compared with the traditional experimental based design of casting [2], the numerical simulation has a great quantity of potential in increasing the productivity of the metal casting industry by shortening time. The microstructure of CI is characterized by graphite lamellas, which disperse into the ferrous matrix. Foundry can influence the nucleation and growth of graphite flakes, and the size and type of graphite flakes enhance the desired properties. The amount of graphite and the size, morphology, and distribution of graphite lamellas are critical in determining the mechanical behavior of CI [3-5].

There is an extensive and increasing effort on the numerical simulation of different processes, including solidification, heating-cooling, and a variety of casting processes [6]. To determine the condition and the optimum values, the simulation of solidification processes is done by computer software or database programming. The program output provides details on determining high stress points [6], porosity distribution and microsegregation, cooling curves, flow rate, module mapping, and solidification processes. Prediction of microstructure evolution in solidification is a key factor in controlling the solidification microstructures, properties, and quality of final casting products [7-9].

The first coupled heat transfer and solidification kinetics in modeling was used in 1985 by Su *et al.* [10] with a finite difference method (FDM). After that, many papers have been published on the micro-modeling of cast iron solidification. However, most of these were in the case of ductile iron. Since the solidification of gray cast iron is affected by the different thermal condition and graphite is in different shapes, modeling of microstructure evolution in this case is somehow complicated.

The data program was written in visual FORTRAN90 in this paper. In the approached program, the macroscopic heat transfer equations were solved in the cast and mold domain

Corresponding author: Masoud Jabbari E-mail: mjab@mek.dtu.dk

with a finite difference method and then coupled with a micro-model to simulate the solidification behavior. The heat capacity (c_p) effective method was used to calculate the latent heat equation. The volume fraction of total γ phase (primary γ and secondary γ in the form of pearlite), graphite, and cementite were all calculated. Finally, this information was connected with the mechanical properties to develop a new equation between the microstructure and the mechanical properties.

2. Macro-modeling

Most metallic materials are produced by melting and solidification, which are generally referred to phase transformations or boundary migration. In solidification of different alloys, three important phenomena should be considered. First, most metals and alloys shrink in the solidification process, which causes shrinkage defects. Second, the latent heat of fusion is released at the solid/liquid interface, which affects the solidification velocity and dependent microstructures. Third, the solute is rejected or absorbed in liquid at the solid/liquid interface during the solidification of alloys, which causes micro- and macro-segregation.

The differential energy balance equation, involving the liberation of latent heat of freezing, is given by

$$\rho c_p \frac{\partial T}{\partial t} = \nabla \cdot (\lambda \Delta T) + \rho H_\mathrm{f} \frac{\partial f_\mathrm{s}}{\partial t} \tag{1}$$

where $\dfrac{\rho H_\mathrm{f} \partial f_\mathrm{s}}{\partial t}$ is the energy generation term, ρ the density, t the time, λ the thermal conductivity of molten metal, H_f the latent heat of freezing, and f_s the volume fraction of solidified metal. By rearranging the energy generation terms, Eq. (2) is shown as

$$\rho H_\mathrm{f} \frac{\partial f_\mathrm{S}}{\partial t} = \rho H_\mathrm{f} \frac{\partial f_\mathrm{s}}{\partial T} \cdot \frac{\partial T}{\partial t} \tag{2}$$

Using Eq. (2) in Eq. (1), Eq. (3) is obtained as

$$\rho \left(c_p - H_\mathrm{f} \frac{\partial f_\mathrm{s}}{\partial t} \right) \frac{\partial T}{\partial t} = \nabla \cdot (\lambda \Delta T) \tag{3}$$

To solve the above equation, the variation of solid volume fraction should be defined as a function of temperature.

The relation between solid volume fraction and temperature may be evaluated from the phase diagrams, except for the congruent solidification in pure metals, eutectic reaction, or peritectic reaction. The solid volume fraction between the liquidus (T_L) to the solidus (T_S) in the mushy zone varies from 0 to 1. In a binary alloy system, the liquidus temperature (T_L^*) is a function of solute concentration in liquid (C_L^*), which depends upon the solute redistribution models [11] as the following equation:

$$T_\mathrm{L}^* = T_\mathrm{L} + m \cdot C_\mathrm{L}^* \tag{4}$$

where T_L is the liquidus temperature for pure metal, m the slope of the liquidus line in the phase diagram, and C_L^* is the concentration in which the liquidus temperatures is aimed to be found.

Because of simplicity, the linear distribution model (LDM) was used in this work to define the variation of solid fraction, shown as the following equation:

$$f_\mathrm{s} = \frac{T_\mathrm{L} - T}{T_\mathrm{L} - T_\mathrm{S}} \tag{5}$$

3. Micro-modeling

In the case of micro-modeling, nucleation and different transformations were considered to predict the solidified phases. One of the most important parameters in determining the characteristics of microstructure evolution is the condition of nucleation in solidification. The solidification of commercial alloys is generally considered as heterogeneous nucleation on the mold surface and in the bulk. Other important parameter in the solidification of gray cast iron is the cooling rate used as a critical parameter in this paper. The amount of gray or white iron is dependent on the isotherms stable temperature (T_st, °C) and metastable temperature (T_mst, °C). These two temperatures are calculated by the chemical composition of the melt and the cooling condition. In this work, for simplicity in calculations, it is assumed that these two temperatures are related to chemical composition, as shown in the following equation [8]:

$$T_\mathrm{st} \text{ and } T_\mathrm{mst} = A + (\%\mathrm{Si})B + (\%\mathrm{Mn})C + (\%\mathrm{P})D \tag{6}$$

where A, B, C, and D are the constants; %Si, %Mn, and %P are the concentration percentage of silicon, manganese, and phosphorus in the melt, respectively. Since there are two different solidification manners, the macro-model equation is separated into two related parts, and the rearranged equation is shown as

$$\rho L \left(\frac{\partial f_\mathrm{s}}{\partial t} \right) = \rho_\mathrm{G} L_\mathrm{G} \left(\frac{\partial f_\mathrm{s}}{\partial t} \right)_\mathrm{G} + \rho_\mathrm{W} L_\mathrm{W} \left(\frac{\partial f_\mathrm{s}}{\partial t} \right)_\mathrm{W} \tag{7}$$

where the subscripts G and W are related to gray and white solidification, respectively.

In this paper, the simple mode of Oldfield's nucleation

model is used, in which nucleation sites are already present in the melt or intentionally added to the melt.

$$N = A + B \cdot R \tag{8}$$

where N is the amount of nucleation per unit face, R the cooling rate, and A and B the nucleation constants. For gray iron, A and B are 10^5 and 3.36×10^4, respectively [12]; and for the white one, it is assumed that A and B are 0 and 10^5, respectively.

In this way, the solid volume fraction is calculated as

$$\left(\frac{\partial f_s}{\partial t}\right) = 4\pi r^2 N \mu \Delta T^2 (1 - f_s) \tag{9}$$

where r represents the actual grain radius, N the nucleation sites, and μ the growth coefficient. The growth coefficient of gray and white eutectic iron is given by Ref. [13].

The simple level rule is used to calculate the different phases. However, since there are two different types of solidification, the calculations for gray iron are obtained from the stable diagram and for the white one from the metastable diagram.

4. Mechanical properties

By modeling the room-temperature microstructure, the final mechanical properties of castings can be predicted. For example, the tensile strength of gray cast iron is affected by graphite flake length, which is related to carbon equivalent, cooling rate, alloying element, and fineness of pearlite. Goodrich *et al.* [14] developed an equation to calculate the ultimate tensile strength (UTS) of gray cast iron, shown as

$$\mathrm{UTS(ksi)} = \left[A + B(\mathrm{CE\%}) + C/(\text{cast bar radius})\right] \tag{10}$$

where %CE is the amount of equivalent carbon, while A, B, and C are the constants that can be calculated from the experiment. Note that A makes the effect on the alloying elements that are present in the cast.

In 1950, Schneidewind and McElwee [15] developed a method based on the chemical composition of gray iron, which can be expressed as

$$\sigma(\mathrm{psi}) = 10^4 \left[b - (2 \times \mathrm{\%CE})\right] \cdot f_1 \cdot f_2 \cdots f_n \tag{11}$$

where σ is the tensile strength, b a constant depending on section size, and f the alloy factors. However, the later works show that the section size is not a good symbol for cooling rate, and the alloy factors are not always appropriate, since they are affected by many metallurgical phenomena.

Furthermore, Serrallach *et al.* [16] performed a statistical analysis to predict the mechanical properties of nodular iron on the basis of the square root of cooling rate, structural features, and alloy composition. However, their work was about nodular solidification, the phase amounts were calculated from the chemical composition, and the solidification behavior (or cooling rate) was not considered.

5. Experimental procedure

A thermal analysis system was conducted for measuring the temperature and related cooling rates. The database was established experimentally for gray iron. The first field of database was a cooling curve. It was really a segment of the cooling curve during the freezing stage from the liquidus temperature (T_{st} and T_{mst}) to the end of eutectic solidification, which was determined by the solidification procedure and related to the solidified microstructure of the sample melt. To study the different solidification behavior on the base of cooling rate, a casting model is designed in the form of steps (S1 to S5), as illustrated in Fig. 1. Full details about the experiment are explained elsewhere by the authors [17].

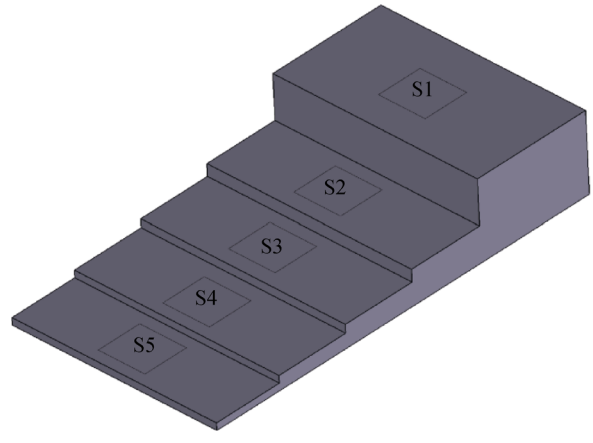

Fig. 1. Model used for casting [17].

6. Results and discussion

The first output of sample modeling is the thermal distribution and cooling rates. The thermal distribution of the sample for the proposed model is illustrated in Fig. 2(a). It is clear that the middle point of step S1 is the last one to solidify in comparison to other sections. Note that in the case of cooling rates, it is assumed that the results are for the geometric center of each section in the modeling; and also in the experiment, the tips of thermocouples are in the same place. Cooling rate data are obtained from the modeling and experiment, respectively, as summarized in Table 1.

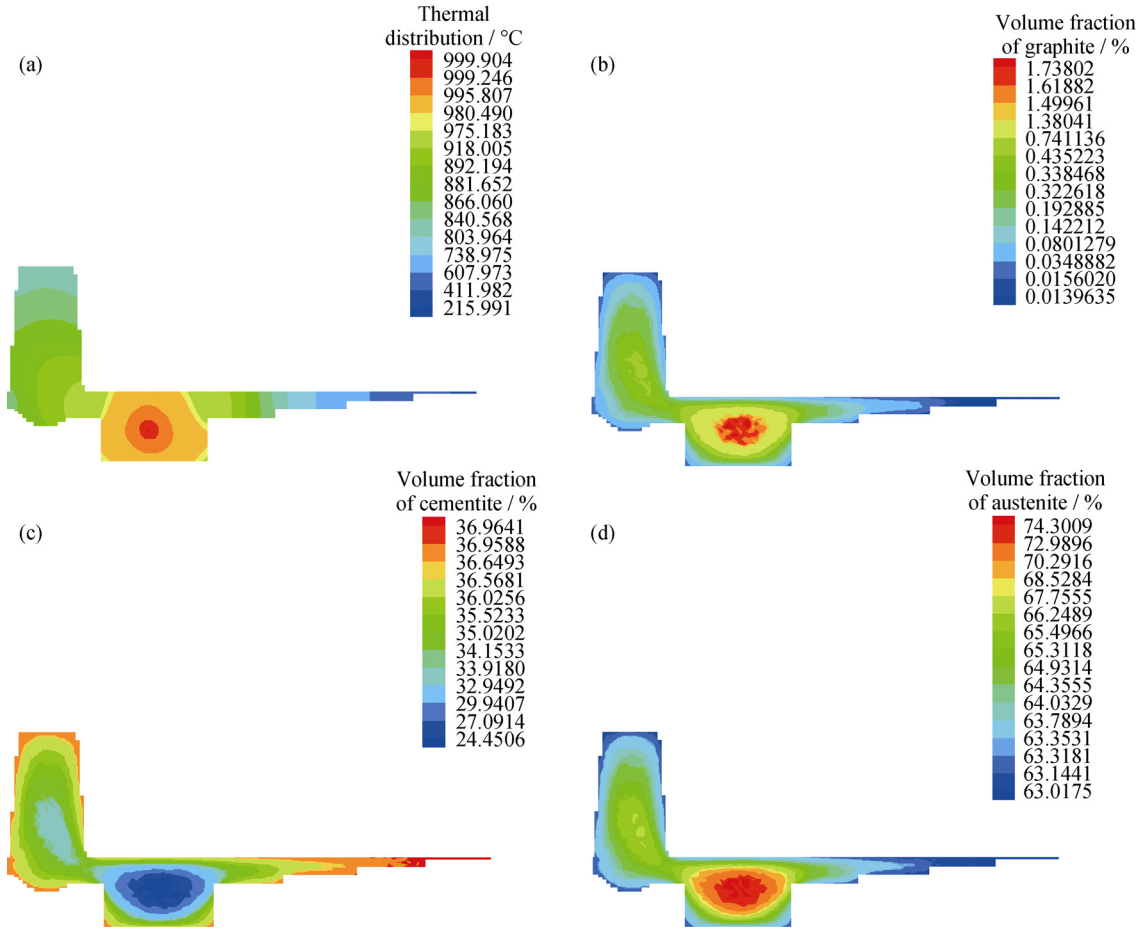

Fig. 2. Contour of modeling: (a) thermal distribution; (b) volume fraction of graphite; (c) volume fraction of cementite; (d) volume fraction of austenite.

Table 1. Cooling rate obtained from modeling and experiment **°C·s^{-1}**

Step	S5	S4	S3	S2	S1
Modeling	15.85	12.07	7.21	2.93	1.18
Experimental	17.67	13.53	8.87	3.14	1.90

Fig. 2(b) shows the contour of graphite distribution in the sample. For the thick section with high module, the volume fraction of graphite is the most. Because of low cooling rate in this section, carbon has enough time to diffuse and forms graphite. The contour of volume fraction for cementite phase distribution is shown in Fig. 2(c). Clearly, for the thin sections with little geometric module, the cementite content is higher. For these sections, the high cooling rates contribute to the high amount of unstable phase (here, cementite phase). The volume fraction distribution of austenite phase is illustrated in Fig. 2(d). The amount of austenite for the thick section with low cooling rate is more than the other sections. Note that in this paper, the amount of austenite was the sum of primary and secondary austenite. Because of this assumption, the volume fraction of austenite contained a fraction of pearlite. Primary austenite is decomposed during the eutectic transformation. When the melt passes the eutectoid line in the phase diagram, the secondary austenite starts to nucleate. Depending on cooling manners and cooling rate, the secondary austenite can be nucleated in the form of reneged austenite or pearlite (ferrite and cementite lamellas). In this paper, the proposed model calculated the amount of whole austenite. Therefore, the thick section had the high amount of austenite in the form of pearlite; for the thin sections, the amount of austenite contained the reneged austenite (ferrite).

Compared the modeling data with the experimental, the image analysis was carried out on different metallographic pictures for each step at the tips of thermocouples. The results are illustrated in Figs. 3-5 graphically. The variation trend of modeling and experiment are the same in all these three phases, but there is a sensible difference between the modeling and experimental results for the amount of austenite phase, and the difference is the most in that of graphite

phase. This may happen since the image analysis tools are on the basis of two phases, the dark and bright phases. Therefore, the image analysis of graphite phase not only contains graphite itself but also cementite (dark phase) in the matrix. Consequently, the amount of graphite phase measured in experiment is higher than that of modeling, and the amount of cementite phase is lower.

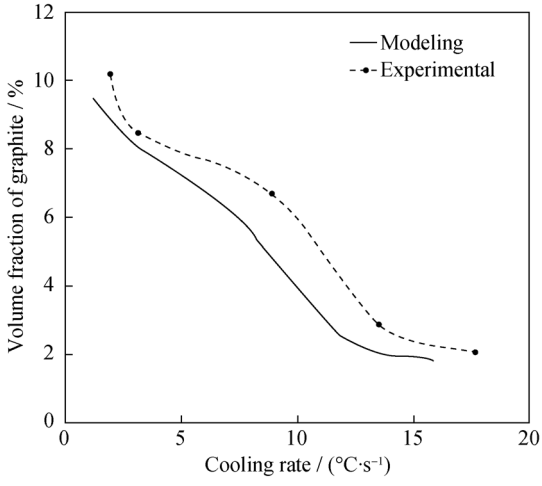

Fig. 3. Comparison of graphite volume fraction obtained from the modeling and experiment data.

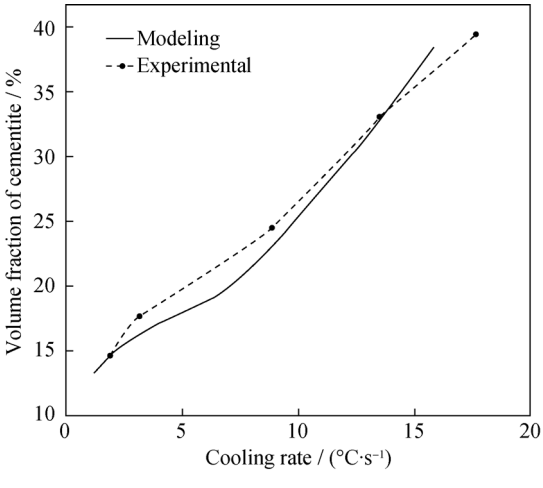

Fig. 4. Comparison of cementite volume fraction obtained from the modeling and experiment data.

The relation between hardness (Brinell hardness, HB) and graphite phase is shown in Fig. 6. As it seen from the figure, the trend of the two curves is the same, except for a small shift forward for the experimental data. This result showed that increasing the graphite fraction causes in a decrease in hardness. This is reasonable that the graphite phase acts as a hole in the metal matrix. Even by increasing the fraction more, the graphite flotation happens, which may

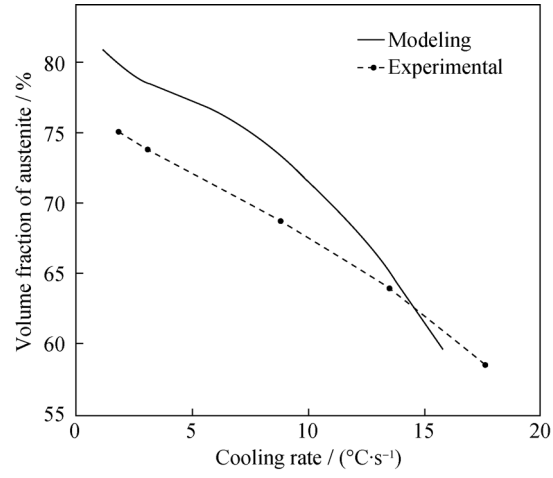

Fig. 5. Comparison of austenite volume fraction obtained from the modeling and experimental data.

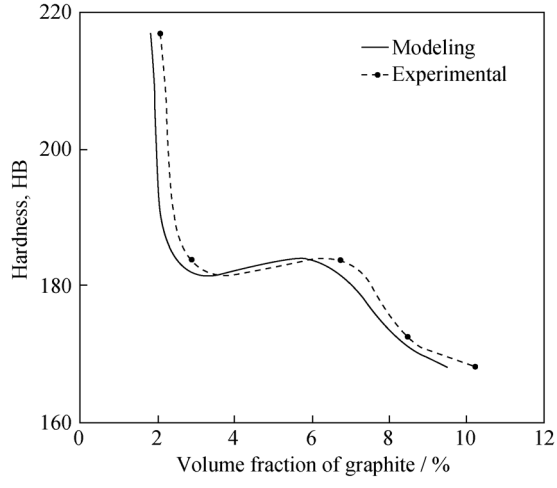

Fig. 6. Relation between the hardness and volume fraction of graphite phase.

cause the start of surface cracks. The smooth increase of hardness could be trade of the behavior of increasing the other phases. The benefit of such a diagram is that, in the same condition of gray cast iron products (on the basis of cooling rate), the amount of graphite phase can be estimated by the hardness value. To approach a good correlation between the hardness and the volume fraction of graphite, a curve is fitted in the range between the modeling and experiment. Moreover, to get better fitting, the axis is changed. The final correlation between graphite phase and hardness is shown as

$$f_g = 0.004\mathrm{HB}^2 - 1.6609\mathrm{HB} + 174.39 \quad (12)$$

where f_g is the volume fraction of graphite phase, and HB is the Brinell hardness.

Note that in this equation, it is assumed that the hardness decreases continuously by increasing the volume fraction of graphite phase.

The effect of the volume fraction of cementite on the hardness is illustrated in Fig. 7, in which the hardness increases with the increase in amount of cementite phase. This phenomenon can be expected by the increase in amount of hard phase. It is known that the increased amount of carbides makes the material more brittle, but the hardness property is exactly related to the amount of hard phase. Besides, during solidification, the amount of total austenite (primary γ and pearlite) increases, which makes the material harder, since a mixture of iron carbide and pearlite is considerably harder than gray iron [17]. Eq. (13) correlates the hardness to the volume fraction of cementite as

$$\mathrm{HB} = 0.0119 f_c^3 - 0.8636 f_c^2 + 20.981 f_c + 11.905 \qquad (13)$$

where f_c stands for the volume fraction of cementite.

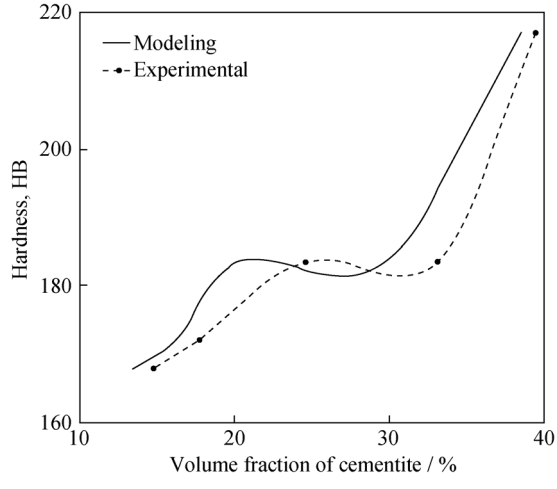

Fig. 7. Relation between the hardness and volume fraction of cementite phase.

The proposed formula on the basis of modeling shows a good agreement with the experimental data. This equation shows the effect of the volume fraction of cementite on the hardness. The inverse mode of this equation can be used for estimating the volume fraction of cementite on the basis of hardness measurement. The proposed formulas can be easily used in the industrial range that was calculated by the authors in the previous work [17]. The good point is that, hardness measurement is the simplest test to carry out. Therefore, by using this kind of mechanical test, the amount of microstructural phases can be measured easily.

7. Conclusions

The solidification behavior of gray cast iron was evaluated numerically. The nucleation and growth theory was used, and cooling rate was implemented as a key factor in the solidified phases. The amount of different phases was calculated using the level rule.

(1) The amount of graphite, cementite, and total austenite can be modeled by an FDM model on the basis of cooling rate and the level rule. As the cooling rate increases, the unstable phases increase. It is notified that increasing the cooling rate results in the increase of cementite phase and the decrease of graphite and austenite phases.

(2) The hardness of gray cast iron decreases as the volume fraction of graphite going up. Increasing the amount of cementite phase results in the improvement in hardness of gray cast iron. The fraction volume of graphite phase can be calculated directly by the following equation on the basis of hardness measurement.

$$\mathrm{HB} = 0.0119 f_c^3 - 0.8636 f_c^2 + 20.981 f_c + 11.905 .$$

Acknowledgments

This work was financially supported by Razi Metallurgical Research Center (RMRC) for the advanced manufacturing and data acquisition system.

References

[1] D.M. Stefanescu, Solidification and modeling of cast iron: a short history of the defining moments, *Mater. Sci. Eng. A*, 413-414(2005), p.322.

[2] M.A. Gafur, M.N. Haque, and K.N. Prabhu, Effect of chill thickness and superheat on casting/chill interfacial heat transfer during solidification of commercially pure aluminium, *J. Mater. Process. Technol.*, 133(2003), p.257.

[3] L. Collini, G. Nicoletto, and R. Konečná, Microstructure and mechanical properties of pearlitic gray cast iron, *Mater. Sci. Eng. A*, 488(2008), p.529.

[4] J.R. Davis, Cast iron, [in] *ASM Specialty Handbook: Cast Irons*, ASM International, Materials Park, Ohio, 1996, p.356.

[5] K. Mills, Metallography and microstructure, [in] G.V. Voort, *ASM Handbook Volume 09: Metallography and Microstructures*, ASM International, Materials Park, Ohio, 1985, p.294.

[6] T.R. Vijayaram, S. Sulaiman, A.M.S. Hamouda, and M.H.M. Ahmad, Numerical simulation of casting solidification in permanent metallic molds, *J. Mater. Process. Technol.*, 178(2006), p.29.

[7] B.Q. LI and P.N. Anyalebechi, A micro/macro model for fluid flow evolution and microstructure formation in solidification processes, *Int. J. Heat Mass Transfer*, 38(1995), p.2367.

[8] A. Shayesteh-Zeraati, H. Naser-Zoshki, and A.R. Kiani- Rashid, Microstructural and mechanical properties (hardness) investigations of Al-alloyed ductile cast iron, *J. Alloys Compd.*, 500(2010), p.129.

[9] R. Venkataramani, R. Simpson, and C. Ravindran, Microstructural modeling of solidification in A356 alloy, *Mater. Charact.*, 35(1995), p.175.

[10] K.C. Su, I. Ohnaka, I. Yamauchhi, and T. Fukusako, Modeling of solidified structure of castings, [in] H. Fredriksson and M. Hillert, *The Physical Metallurgy of Cast Iron*, Elsevier, Amsterdam, 1985, p.181.

[11] M.C. Flemings, Solidification processing, *Metall. Trans.*, 5(1974), p.2121.

[12] H. Fredriksson and M. Hillert, The physical metallurgy of cast iron, [in] *Proceedings of the Third International Symposium on the Physical Metallurgy of Cast Iron*, Stockholm, Sweden, 1984, p.273.

[13] H. Tian and D.M. Stefanescu, Modeling of casting, welding and advanced solidification processes VI, [in] *Proceedings of the 6th Conference in a Series on Modeling, Casting, and Welding Processes*, Florida, USA, 1993, p.639.

[14] G.M. Goodrich and W.F. Shaw, New formula equates tensile strength of gray iron, *Mod. Cast*, No.10, 1992, p.219.

[15] R. Schneidewind and R.G. McElwee, Composition and properties of gray iron: Part I and II, *AFS Trans.*, 58(1950), p.312.

[16] J. Serrallach, J. Lacaze, J. Sertucha, R. Suárez, and A. Monzón, Effect of selected alloying elements on mechanical properties of pearlitic nodular cast irons, *Key Eng. Mater.*, 457(2011), p.361.

[17] M.M. Jabbari Behnam, P. Davami, and N. Varahram, Effect of cooling rate on microstructure and mechanical properties of gray cast iron, *Mater. Sci. Eng. A*, 528(2010), p.583.